

# A theory of state-to-state transitions based on the framework of classical reaction dynamics

Kento Kasahara,<sup>1, a)</sup> Ryo Okabe,<sup>1</sup> Chia-en A. Chang,<sup>2, b)</sup> Toshifumi Mori,<sup>3, c)</sup> and Nobuyuki Matubayasi<sup>1, d)</sup>

<sup>1)</sup>Division of Chemical Engineering, Graduate School of Engineering Science, The University of Osaka, Toyonaka, Osaka 560-8531, Japan

<sup>2)</sup>Department of Chemistry, University of California at Riverside, Riverside, California 92521, United States

<sup>3)</sup>Institute for Materials Chemistry and Engineering, Kyushu University, Kasuga, Fukuoka 816-8580, Japan

We propose a new method to describe the population dynamics of distinct configurational states based on a continuous-time description of state-to-state transitions. According to classical reaction dynamics theory, the probability density associated with a given state obeys the Liouville equation, including influx from and efflux to neighboring states. By introducing a Markov approximation for the crossing of boundaries separating the states, tractable integral equations governing the state populations are derived. Once the time-dependent quantities appearing in these equations are evaluated, the population dynamics on long timescales can be obtained. Because these quantities depend only on a few states in the local neighborhood of a given state, they can be computed using a set of short-timescale molecular dynamics (MD) simulations. We apply the present method to the binding and unbinding kinetics of  $\text{CH}_4/\text{CH}_4$ ,  $\text{Na}^+/\text{Cl}^-$ , and 18-crown-6-ether (crown ether)/ $\text{K}^+$  in water. For both kinetics, the time constants estimated from the present method are almost comparable to those obtained from brute-force MD simulations. The required timescale of each MD trajectory in the present method is approximately two orders of magnitude shorter than that in the brute-force MD approach in the crown ether/ $\text{K}^+$  system. This reduction in the trajectory timescale enables applications to complex binding and unbinding systems whose characteristic timescales are far beyond those directly accessible by brute-force MD simulations.

## I. INTRODUCTION

The dynamics of proteins, including folding and unfolding as well as ligand binding and unbinding, proceed through a number of intermediate states, which are closely related to cellular biological functions. Recent advances in single-molecule spectroscopy techniques allow the measurement of such state-to-state transitions.<sup>1</sup> For instance, the folding and unfolding rates of the WW domain of formin-binding protein were successfully determined through the Förster resonance energy transfer (FRET) spectroscopy.<sup>2</sup> In the case of protein–ligand binding and unbinding, surface plasmon resonance (SPR) measurement is a powerful tool for analyzing these kinetics.<sup>3–5</sup> To gain further structural insight into the dynamics mentioned above, molecular dynamics (MD) simulations<sup>6,7</sup> have played a central role, as molecular motions can be traced at atomistic resolution. The accessible timescale using standard computers is limited to the submillisecond regime, however, and advanced techniques based on statistical mechanics have been developed to elucidate dynamics occurring on longer timescales.<sup>8,9</sup>

To elucidate the structural dynamics of the biological systems based on MD simulations, the Markov state

model (MSM) has been widely utilized.<sup>10–12</sup> This method enables the description of long-timescale structural dynamics of the target molecule based on transitions between states that characterize distinct stable structures. The development of methodologies combined with enhanced sampling techniques is an important advancement for the MSM method.<sup>13–17</sup> Systematic schemes for defining Markov states have also been extensively developed, greatly expanding the versatility of the MSM method.<sup>18–20</sup> A practical limitation is the need to introduce a coarse-grained timescale, namely a lag time, in computing transition probabilities to ensure Markovianity of the state-to-state transitions. It is known that the resulting kinetic properties, such as rate constants, can be sensitive to the choice of the lag time.<sup>21</sup> Accordingly, extending the method to overcome the limitation remains an important topic. The history-augmented MSM (haMSM) method<sup>22,23</sup> was developed to address this issue by partially accounting for non-Markovian effects. The generalized master equation (GME) approach<sup>24,25</sup>, which practically constructs the memory kernel associated with the state-to-state transitions from MD trajectories, is also a promising framework for enabling robust evaluation of the kinetic properties of interest.

Milestoning theory<sup>26</sup> is an alternative of the MSM method to evaluate the kinetics of state-to-state transitions from a number of short MD trajectories. The theory originally formulated by Faradjian and Elber treats a continuous-time description of transitions between the boundaries (referred to as milestones) that separate states.<sup>27</sup> In this approach, the time evolution of the populations on the milestones is described. The mileston-

<sup>a)</sup>Author to whom correspondence should be addressed: kasahara@cheng.es.osaka-u.ac.jp

<sup>b)</sup>Electronic mail: chiaenc@ucr.edu

<sup>c)</sup>Electronic mail: toshi\_mori@cm.kyushu-u.ac.jp

<sup>d)</sup>Electronic mail: nobuyuki@cheng.es.osaka-u.ac.jp

ing theory has been extended to make it amenable to MD simulations by eliminating the continuous-time description while retaining the accuracy in terms of the mean first passage time (MFPT).<sup>28–34</sup> Markovian milestone with Voronoi tessellations (MMVT) method<sup>29</sup> is a representative example of such extensions. Weighted ensemble milestone (WEM)<sup>30,31</sup> incorporates the weighted ensemble (WE) method,<sup>35–37</sup> an enhanced sampling method with unbiased MD simulations, into the milestone theory, reducing the computational cost required for the milestone theory. Unlike the MSM method, the timescale of the state-to-state transitions is determined for each pair of adjacent milestones based on MD simulations, eliminating the need to set a lag time. On the other hand, the information on a configuration state is represented only with the surrounding milestones. Thus, the setting of milestones is crucial not only for achieving accurate kinetic predictions but also for enabling meaningful structural interpretation. Furthermore, since the free-energy profile obtained from the steady flux is defined with respect to the milestone index, it is difficult to directly compare the free-energy difference between the two target milestones with the experimentally measured value.

Classical reaction dynamics theory has been established to rigorously elucidate molecular kinetic processes.<sup>38–40</sup> In the diffusion-influenced reaction (DIR) theories, the time evolution of the reactant distribution is expressed as transport equations, such as diffusion equation, with the reaction terms for describing reaction events.<sup>41,42</sup> The modern DIR theory allows the Liouville equation of the system of interest to be employed as the transport equation, thereby expanding the applicability of the theoretical framework.<sup>43</sup> By regarding a binding event as a type of reaction process, the framework of DIR theory can be employed to describe binding kinetics. The returning probability theory is such a theory, which characterizes binding kinetics in terms of the thermodynamic and dynamic properties of a reactive state that exists during the binding process.<sup>43–45</sup> Very recently, we formulated the returning probability theory for membrane permeation.<sup>46</sup> As demonstrated by these developments, the framework of classical reaction dynamics is expected to be useful for constructing methodologies to describe a wide class of molecular kinetics.

Here, we develop a methodology based on the classical dynamics theory to describe the state-to-state transitions. The integral equations of the population dynamics are derived through a systematic approximation. Conceptually, the derived equations are similar to those used in the original milestone theory<sup>27,47</sup>, but they describe the populations of states rather than those on boundaries (milestones). This feature makes it possible to compute various types of time-correlation functions related to populations, such as the hydrogen-bond time-correlation function<sup>48,49</sup> and first-passage time distribution functions,<sup>50,51</sup> without modifying the original definitions of these functions. The time-dependent functions

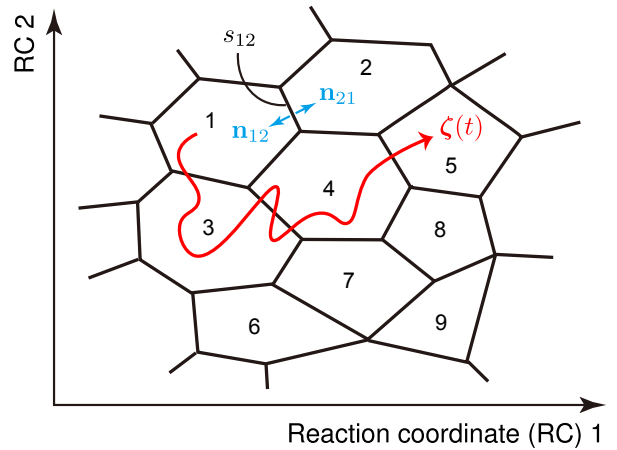


FIG. 1. Reaction-coordinate space and its division into a set of states,  $\Upsilon_1, \Upsilon_2, \dots$ . The normal vector on the boundary between states  $i$  and  $j$  is defined as  $\mathbf{n}_{ij}$ , where the vector points toward state  $i$ .  $s_{ij}$  signifies the boundary separating states  $i$  and  $j$ .

for a state involved in the derived equations are described only by a limited number of states in the local neighborhood, and thus their evaluation is possible using a number of short-timescale MD trajectories.

We apply the developed method to the binding and unbinding kinetics of three aqueous systems:  $\text{CH}_4/\text{CH}_4$ ,  $\text{Na}^+/\text{Cl}^-$ , and 18-crown-6 ether (crown ether)/ $\text{K}^+$ . Since the timescales of binding and unbinding for these systems are accessible to MD simulations, as demonstrated by Zwier *et al.*,<sup>52</sup> these systems are suitable for verifying the accuracy of kinetic quantities estimated from the present method. We perform short-timescale MD simulations to compute the quantities required for the present method. In addition, we conduct brute-force MD simulations to directly evaluate the kinetic quantities without resorting to any approximations, for comparison.

## II. THEORY

### A. State definition based on reaction coordinate

We consider the dynamics of the system of interest along a reaction coordinate. Let  $\hat{\Gamma}(t)$  be the phase-space coordinate at time  $t$ , and the value of the reaction coordinate is uniquely determined from  $\hat{\Gamma}(t)$  as  $\zeta(t) = \zeta(\hat{\Gamma}(t))$ . Then, the space spanned by the reaction coordinate is divided into a set of states,  $\Upsilon_1, \Upsilon_2, \dots$  (Fig. 1). The set of labels for the states neighboring state  $j$  is defined as  $\mathcal{N}_j$ . We also define the normal vector on the boundary between states  $i$  and  $j$  as  $\mathbf{n}_{ij}$ , where the vector points from state  $j$  to state  $i$ . By definition, this implies  $\mathbf{n}_{ij} = -\mathbf{n}_{ji}$ .

A key quantity in state-to-state transition dynamics is the probability of being in state  $j$  at time  $t$ , given a certain initial condition, denoted as  $P_j(t)$ . When the system is initially in equilibrium and in state I ( $\boldsymbol{\Upsilon}_I$ ),  $P_j(t)$  can be expressed as

$$P_j(t) = \frac{\langle \Theta_j(\boldsymbol{\zeta}(t)) \Theta_I(\boldsymbol{\zeta}(0)) \rangle}{\langle \Theta_I(\boldsymbol{\zeta}(0)) \rangle}. \quad (1)$$

Here,  $\langle \cdots \rangle$  indicates the ensemble average in equilibrium, and  $\Theta_k(\boldsymbol{\zeta}(t))$  ( $k = j$  or I) is the characteristic function for state  $k$  defined as

$$\Theta_k(\boldsymbol{\zeta}(t)) = \begin{cases} 1 & \boldsymbol{\zeta}(t) \in \boldsymbol{\Upsilon}_k \\ 0 & \boldsymbol{\zeta}(t) \notin \boldsymbol{\Upsilon}_k \end{cases}. \quad (2)$$

We suppose that state I consists of multiple states, and the set of labels for these states is denoted as  $\mathcal{M}_I$ . Thus,  $\Theta_I(\boldsymbol{\zeta}(t))$  can be described as

$$\Theta_I(\boldsymbol{\zeta}(t)) = \sum_{k \in \mathcal{M}_I} \Theta_k(\boldsymbol{\zeta}(t)). \quad (3)$$

For later convenience, let us introduce the following notation for the conditional ensemble average.

$$\langle \cdots \rangle_I = \frac{\langle (\cdots) \Theta_I(\boldsymbol{\zeta}(0)) \rangle}{\langle \Theta_I(\boldsymbol{\zeta}(0)) \rangle}. \quad (4)$$

By using this notation, Eq. (1) can be rewritten as  $P_j(t) = \langle \Theta_j(\boldsymbol{\zeta}(t)) \rangle_I$ .

## B. Reaction model

In this subsection, we describe a reaction model that allows population exchange, including efflux and influx, between neighboring states. This model is an extension of those used in bimolecular diffusion-influenced reaction theory.<sup>41,43,53</sup>

Let  $\hat{\Psi}(\boldsymbol{\Gamma}, t)$  be the instantaneous phase-space ( $\boldsymbol{\Gamma}$ ) probability density over the whole phase space at time  $t$ . The time development of  $\hat{\Psi}(\boldsymbol{\Gamma}, t)$  is given by

$$\frac{\partial}{\partial t} \hat{\Psi}(\boldsymbol{\Gamma}, t) = -\mathcal{L} \hat{\Psi}(\boldsymbol{\Gamma}, t), \quad (5)$$

where  $\mathcal{L}$  is the Liouville operator. The normalization condition of  $\hat{\Psi}(\boldsymbol{\Gamma}, t)$  is

$$\int d\boldsymbol{\Gamma} \hat{\Psi}(\boldsymbol{\Gamma}, t) = 1. \quad (6)$$

Then, the probability density for state  $j$  is defined as

$$\hat{f}_j(\boldsymbol{\Gamma}, t) = \hat{\Psi}(\boldsymbol{\Gamma}, t) \Theta_j(\boldsymbol{\zeta}). \quad (7)$$

In the above expression, the value of the reaction coordinate at  $\boldsymbol{\Gamma}$ ,  $\boldsymbol{\zeta}(\boldsymbol{\Gamma})$ , is denoted simply as  $\boldsymbol{\zeta}$ . Evidently, Eq. (7) satisfies the following relationship:

$$\hat{\Psi}(\boldsymbol{\Gamma}, t) = \sum_j \hat{f}_j(\boldsymbol{\Gamma}, t). \quad (8)$$

The values of  $\hat{f}_j(\boldsymbol{\Gamma}, t)$  at the boundaries are set to

$$\hat{f}_j(\boldsymbol{\Gamma}, t) = \begin{cases} \hat{f}_i(\boldsymbol{\Gamma}, t) & \text{for } \boldsymbol{\zeta} \in s_{ij}, \dot{\boldsymbol{\zeta}} \cdot \mathbf{n}_{ij} < 0 \\ \hat{f}_j(\boldsymbol{\Gamma}, t) & \text{for } \boldsymbol{\zeta} \in s_{ij}, \dot{\boldsymbol{\zeta}} \cdot \mathbf{n}_{ij} > 0 \end{cases}. \quad (9)$$

Here,  $s_{ij}$  is the boundary separating states  $i$  and  $j$ . The above condition specifies the detailed definition of states based on the velocity,  $\dot{\boldsymbol{\zeta}}$ , at the boundaries. The problem of solving the transport equation with a boundary can be converted into that of solving a transport equation in which the boundary condition is replaced by reaction sink terms, as demonstrated by Molski<sup>53</sup> for the Fokker-Planck equation. We extend Molski's method to derive the governing equation of  $\hat{f}_j(\boldsymbol{\Gamma}, t)$  from Eqs. (5)-(9), as described below.

Since  $\hat{\Psi}(\boldsymbol{\Gamma}, t)$  and  $\hat{f}_j(\boldsymbol{\Gamma}, t)$  have  $\boldsymbol{\Gamma}$  (and  $\boldsymbol{\zeta}$ ) as field variables and depend on time only through the second argument  $t$ , let us notify

$$\frac{\partial}{\partial t} \hat{f}_j(\boldsymbol{\Gamma}, t) = \Theta_j(\boldsymbol{\zeta}) \frac{\partial}{\partial t} \hat{\Psi}(\boldsymbol{\Gamma}, t), \quad (10)$$

and thus substituting Eq. (5) into the above equation yields

$$\begin{aligned} \frac{\partial}{\partial t} \hat{f}_j(\boldsymbol{\Gamma}, t) &= -\Theta_j(\boldsymbol{\zeta}) \mathcal{L} \hat{\Psi}(\boldsymbol{\Gamma}, t) \\ &= -\mathcal{L} \hat{f}_j(\boldsymbol{\Gamma}, t) + \hat{\Psi}(\boldsymbol{\Gamma}, t) \mathcal{L} \Theta_j(\boldsymbol{\zeta}), \end{aligned} \quad (11)$$

where we have used the product rule for derivatives

$$\mathcal{L} \hat{f}_j(\boldsymbol{\Gamma}, t) = \Theta_j(\boldsymbol{\zeta}) \mathcal{L} \hat{\Psi}(\boldsymbol{\Gamma}, t) + \hat{\Psi}(\boldsymbol{\Gamma}, t) \mathcal{L} \Theta_j(\boldsymbol{\zeta}). \quad (12)$$

Applying the Liouville operator ( $\mathcal{L}$ ) to  $\Theta_j(\boldsymbol{\zeta})$  gives

$$\begin{aligned} \mathcal{L} \Theta_j(\boldsymbol{\zeta}) &= (\mathcal{L} \boldsymbol{\zeta}) \cdot \sum_{i \in \mathcal{N}_j} (-\mathbf{n}_{ij}) \delta_{ij}^s(\boldsymbol{\zeta}) \\ &= - \sum_{i \in \mathcal{N}_j} (\dot{\boldsymbol{\zeta}} \cdot \mathbf{n}_{ij}) \delta_{ij}^s(\boldsymbol{\zeta}), \end{aligned} \quad (13)$$

where we have used the relationship given by  $\mathcal{L} \boldsymbol{\zeta} = \dot{\boldsymbol{\zeta}}$ .  $\delta_{ij}^s(\boldsymbol{\zeta})$  is the surface delta function for boundary  $s_{ij}$ , defined as the function satisfying

$$\int d\boldsymbol{\xi} A(\boldsymbol{\xi}) \delta_{ij}^s(\boldsymbol{\xi}) = \int_{s_{ij}} d\sigma A(\boldsymbol{\xi}), \quad (14)$$

for an arbitrary function  $A$ . Here,  $\int_{s_{ij}} d\sigma$  is the surface integral over  $s_{ij}$ . By substituting Eq. (13) into Eq. (11), one can obtain

$$\begin{aligned} \frac{\partial}{\partial t} \hat{f}_j(\boldsymbol{\Gamma}, t) &= -\mathcal{L} \hat{f}_j(\boldsymbol{\Gamma}, t) \\ &\quad - \sum_{i \in \mathcal{N}_j} (\dot{\boldsymbol{\zeta}} \cdot \mathbf{n}_{ij}) \delta_{ij}^s(\boldsymbol{\zeta}) \hat{\Psi}(\boldsymbol{\Gamma}, t). \end{aligned} \quad (15)$$

Furthermore, according to the boundary condition (Eq. (9)), the above equation can be rewritten as

$$\begin{aligned} \frac{\partial}{\partial t} \hat{f}_j(\boldsymbol{\Gamma}, t) &= -\mathcal{L} \hat{f}_j(\boldsymbol{\Gamma}, t) \\ &\quad - \sum_{i \in \mathcal{N}_j} S_{ij}(\boldsymbol{\zeta}, \dot{\boldsymbol{\zeta}}) \hat{f}_j(\boldsymbol{\Gamma}, t) \\ &\quad + \sum_{k \in \mathcal{N}_j} S_{jk}(\boldsymbol{\zeta}, \dot{\boldsymbol{\zeta}}) \hat{f}_k(\boldsymbol{\Gamma}, t). \end{aligned} \quad (16)$$

Here,  $S_{ij}$  is the reaction sink function corresponding to the efflux state  $j$  to state  $i$ , defined using the Heaviside step function ( $H(x)$ ) as

$$S_{ij}(\boldsymbol{\zeta}, \dot{\boldsymbol{\zeta}}) = (\dot{\boldsymbol{\zeta}} \cdot \mathbf{n}_{ij}) H(\dot{\boldsymbol{\zeta}} \cdot \mathbf{n}_{ij}) \delta_{ij}^s(\boldsymbol{\zeta}). \quad (17)$$

Eq. (17) expresses the condition in which efflux occurs when the velocity  $\dot{\boldsymbol{\zeta}}$  is directed toward state  $i$  on boundary  $s_{ij}$ . The population entering state  $i$  from state  $j$  at  $\boldsymbol{\zeta} \in s_{ij}$  during the time interval from  $t$  to  $t+dt$ ,  $\hat{Q}_{ij}(\boldsymbol{\Gamma}, t)$ , is given by

$$\hat{Q}_{ij}(\boldsymbol{\Gamma}, t) = S_{ij}(\boldsymbol{\zeta}, \dot{\boldsymbol{\zeta}}) \hat{f}_j(\boldsymbol{\Gamma}, t). \quad (18)$$

By introducing the Liouville operator incorporating the efflux

$$\mathcal{L}_j = \mathcal{L} + \sum_{i \in \mathcal{N}_j} S_{ij}, \quad (19)$$

and multiplying the both sides of Eq. (16) by  $e^{\mathcal{L}_j t}$ , one can obtain

$$\frac{\partial}{\partial t} \left[ e^{\mathcal{L}_j t} \hat{f}_j(\boldsymbol{\Gamma}, t) \right] = \sum_{k \in \mathcal{N}_j} e^{\mathcal{L}_j t} \hat{Q}_{jk}(\boldsymbol{\Gamma}, t). \quad (20)$$

Integrating the above equation over time yields the following formal solution of Eq. (16).

$$\begin{aligned} \hat{f}_j(\boldsymbol{\Gamma}, t) &= e^{-\mathcal{L}_j t} \hat{f}_j(\boldsymbol{\Gamma}, 0) \\ &\quad + \sum_{k \in \mathcal{N}_j} \int_0^t d\tau e^{-\mathcal{L}_j(t-\tau)} \hat{Q}_{jk}(\boldsymbol{\Gamma}, \tau). \end{aligned} \quad (21)$$

The first term on the right-hand side of Eq. (21) represents the population that remains in state  $j$  from the time interval from 0 to  $t$ . The integrand of the second term is the population that arrives at state  $j$  from state  $k$  during the time interval from  $\tau$  to  $\tau + d\tau$  and remains in state  $j$  until time  $t$ . Substituting Eq. (21) into Eq. (18) leads to

$$\begin{aligned} \hat{Q}_{ij}(\boldsymbol{\Gamma}, t) &= S_{ij}(\boldsymbol{\zeta}, \dot{\boldsymbol{\zeta}}) e^{-\mathcal{L}_j t} \hat{f}_j(\boldsymbol{\Gamma}, 0) \\ &\quad + \sum_{k \in \mathcal{N}_j} \int_0^t d\tau S_{ij}(\boldsymbol{\zeta}, \dot{\boldsymbol{\zeta}}) e^{-\mathcal{L}_j(t-\tau)} \hat{Q}_{jk}(\boldsymbol{\Gamma}, \tau). \end{aligned} \quad (22)$$

### C. Coarse-grained reaction dynamics

We derive a coarse-grained description of reaction dynamics, where state-to-state transitions are described without using the phase-space coordinate,  $\boldsymbol{\Gamma}$ .

According to Eqs. (1), (4), and (7),  $P_j(t)$  is expressed as

$$P_j(t) = \int d\boldsymbol{\Gamma} \left\langle \hat{f}_j(\boldsymbol{\Gamma}, t) \right\rangle_I. \quad (23)$$

For simplicity of notations, we introduce

$$\langle \langle \cdots \rangle \rangle = \int d\boldsymbol{\Gamma} \langle \cdots \rangle, \quad (24)$$

$$\langle \langle \cdots \rangle \rangle_I = \int d\boldsymbol{\Gamma} \langle \cdots \rangle_I, \quad (25)$$

Using the above notations,  $P_j(t)$  can be rewritten as  $P_j(t) = \langle \langle \hat{f}_j(\boldsymbol{\Gamma}, t) \rangle \rangle_I$ . Furthermore, one can express the governing equation of  $P_j(t)$  from Eq. (21) as

$$\begin{aligned} P_j(t) &= P_j^0(t) \\ &\quad + \sum_{k \in \mathcal{N}_j} \int_0^t d\tau \left\langle \left\langle e^{-\mathcal{L}_j(t-\tau)} \hat{Q}_{jk}(\boldsymbol{\Gamma}, \tau) \right\rangle \right\rangle_I, \end{aligned} \quad (26)$$

where  $P_j^0(t)$  is defined as

$$P_j^0(t) = \langle \langle e^{-\mathcal{L}_j t} \hat{f}_j(\boldsymbol{\Gamma}, 0) \rangle \rangle_I. \quad (27)$$

The time propagator,  $e^{-\mathcal{L}_j t}$ , acting on the phase-space density  $\hat{f}_j$  generates the time development of  $\hat{f}_j$  while the system remains in state  $j$ , and the value of  $\hat{f}_j$  vanishes once the system crosses into other states. Thus,  $P_j^0(t)$  represents the population that was initially in state  $j$  and remains there without visiting other states before time  $t$ . Note that  $P_j^0(t)$  is nonzero only if  $j \in \mathcal{M}_I$  and its initial value is

$$P_j^0(0) = \frac{\langle \Theta_j(\boldsymbol{\zeta}) \rangle}{\langle \Theta_I(\boldsymbol{\zeta}) \rangle} \equiv w_j. \quad (28)$$

The integrand of the second term on the right-hand side of Eq. (26) represents two successive processes: crossing from state  $k$  to state  $j$  during the time interval from  $\tau$  to  $\tau + d\tau$ , followed by retention in state  $j$  up to time  $t$ . As a lowest-order approximation, we assume a Markov property such that the processes before and after crossing a boundary are uncorrelated. Under this assumption, the dynamics of the population originating from neighboring states is treated as a single process until it crosses the surrounding boundaries. Then, the integrand of the second term in Eq. (26) can be approximated as

$$\langle \langle e^{-\mathcal{L}_j(t-\tau)} \hat{Q}_{jk}(\boldsymbol{\Gamma}, \tau) \rangle \rangle_I \approx M_{jk}(t-\tau) Q_{jk}(\tau), \quad (29)$$

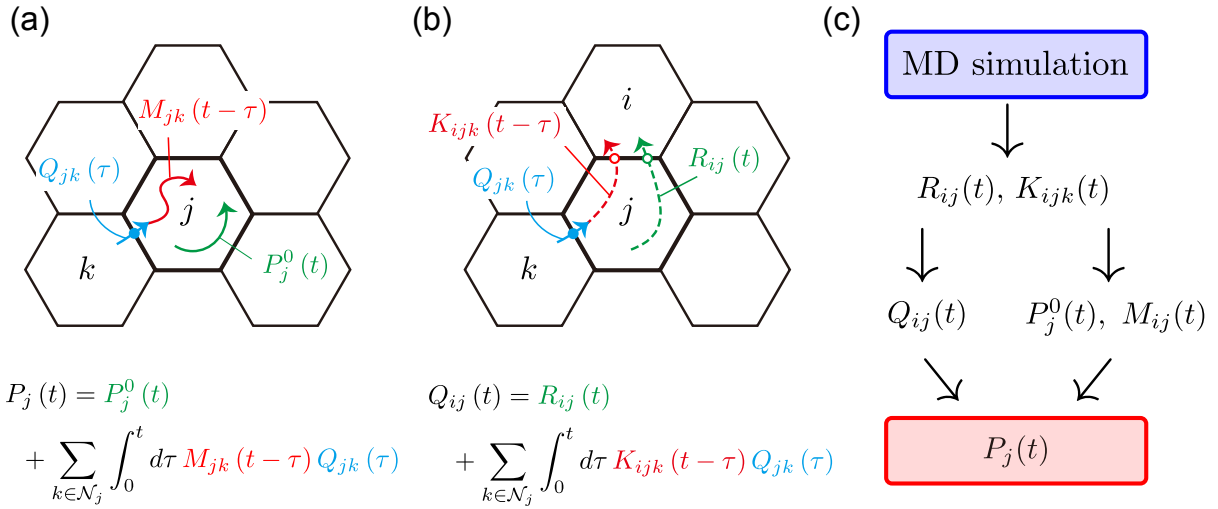


FIG. 2. Schemes of the governing equations for (a)  $P_j(t)$ , (b)  $Q_{ij}(t)$ , and (c) procedure for computing  $P_j(t)$  from MD simulations.

where

$$Q_{ij}(t) = \left\langle \left\langle \hat{Q}_{ij}(\Gamma, t) \right\rangle \right\rangle_I, \quad (30)$$

$$M_{ij}(t) = \frac{\left\langle e^{-\mathcal{L}_j t} S_{ij}(\zeta, \dot{\zeta}) \right\rangle}{\left\langle S_{ij}(\zeta, \dot{\zeta}) \right\rangle}. \quad (31)$$

$Q_{ij}(t)$  represents the efflux from state  $j$  to state  $i$  during the time interval from  $t$  to  $t + dt$ , while  $M_{ij}(t)$  denotes the population of state  $i$  that arrived from state  $j$  during the time interval from 0 to  $dt$  and remains in state  $i$  at time  $t$  (Fig. 2(a)). Since  $M_{ij}(t)$  is conditioned by  $\langle S_{ij}(\zeta, \dot{\zeta}) \rangle$ , its initial value is unity. Eq. (29) implies that the population crossing from state  $k$  to state  $j$  during the time interval from  $\tau$  to  $\tau + d\tau$  and the subsequent retention of the population up to time  $t$  are described by  $Q_{jk}(\tau)$  and  $M_{jk}(t-\tau)$ , respectively, and that the retention process proceeds independently of the crossing event. The approximation introduced in Eq. (29) is valid when each state is sufficiently wide. Substituting Eq. (29) into Eq. (26) yields

$$P_j(t) = P_j^0(t) + \sum_{k \in \mathcal{N}_j} \int_0^t d\tau M_{jk}(t-\tau) Q_{jk}(\tau). \quad (32)$$

Since the time evolution of  $P_j^0(t)$  and  $M_{jk}(t)$  is governed by  $e^{-\mathcal{L}_j t}$ , only the population that remains within state  $j$  is taken into account. In contrast,  $P_j(t)$  accounts for the population in state  $j$  irrespective of how it arrives there. The above feature of  $P_j^0(t)$  and  $M_{jk}(t)$  ensures the much faster convergence of these functions to zero than that of  $P_j(t)$ , enabling the computation of  $P_j^0(t)$  and  $M_{jk}(t)$  using short-timescale MD trajectories. Thus,

once a scheme for computing  $Q_{ij}(t)$  is established,  $P_j(t)$  can be computed on a long timescale using the above equation.

By definition of  $Q_{ij}(t)$  (Eq. (30)), the governing equation of  $Q_{ij}(t)$  is obtained by taking ensemble average of Eq. (22) and integration over  $\Gamma$  as

$$Q_{ij}(t) = R_{ij}(t) + \sum_{k \in \mathcal{N}_j} \int_0^t d\tau \left\langle \left\langle S_{ij}(\zeta, \dot{\zeta}) e^{-\mathcal{L}_j(t-\tau)} \hat{Q}_{jk}(\Gamma, \tau) \right\rangle \right\rangle_I. \quad (33)$$

Here,  $R_{ij}(t)$  is the population that was initially localized in state  $j$  and crosses from state  $j$  to state  $i$  for the first time during the time interval from  $t$  to  $t + dt$ .

$$R_{ij}(t) = \left\langle \left\langle S_{ij}(\zeta, \dot{\zeta}) e^{-\mathcal{L}_j t} \hat{f}_j(\Gamma, 0) \right\rangle \right\rangle_I. \quad (34)$$

The second term on the right-hand side of Eq. (33) implies that the population comes from state  $k$  to state  $j$  during time  $\tau$  to  $\tau + d\tau$ , followed by the crossing to state  $i$  during time  $t$  to  $t + dt$ . Similar to Eq. (29), the second term on the right-hand side of Eq. (33) can be simplified using the Markov approximation as

$$\left\langle \left\langle S_{ij}(\zeta, \dot{\zeta}) e^{-\mathcal{L}_j(t-\tau)} \hat{Q}_{jk}(\Gamma, \tau) \right\rangle \right\rangle_I \approx K_{ijk}(t-\tau) Q_{jk}(\tau), \quad (35)$$

where

$$K_{ijk}(t) = \frac{\left\langle S_{ij}(\zeta, \dot{\zeta}) e^{-\mathcal{L}_j t} S_{jk}(\zeta, \dot{\zeta}) \right\rangle}{\left\langle S_{jk}(\zeta, \dot{\zeta}) \right\rangle}, \quad (36)$$

represents the population that arrived at state  $j$  from state  $k$  during the time interval from 0 to  $dt$  and crosses from state  $j$  to state  $i$  for the first time during the time interval from  $t$  to  $t+dt$  (Fig. 2(b)). Applying the Markov approximation (Eq. (35)) to Eq. (33) leads to

$$Q_{ij}(t) = R_{ij}(t) + \sum_{k \in \mathcal{N}_j} \int_0^t d\tau K_{ijk}(\tau) Q_{jk}(\tau). \quad (37)$$

By using this equation, one can calculate  $Q_{ij}(t)$  once  $R_{ij}(t)$  and  $K_{ijk}(t)$  are obtained from MD simulations. Furthermore,  $P_j^0(t)$  and  $M_{jk}(t)$  can be calculated from  $R_{ij}(t)$  and  $K_{ijk}(t)$ , respectively, as described in Appendix A. The resulting relationships between  $P_j^0(t)$  and  $R_{ij}(t)$ , and between  $M_{jk}(t)$  and  $K_{ijk}(t)$ , are given by

$$P_j^0(t) = w_j - \sum_{i \in \mathcal{N}_j} \int_0^t d\tau R_{ij}(\tau), \quad (38)$$

$$M_{jk}(t) = 1 - \sum_{i \in \mathcal{N}_j} \int_0^t d\tau K_{ijk}(\tau). \quad (39)$$

Accordingly, it is possible to evaluate  $P_j(t)$  through Eqs. (32) and (37) after computing  $R_{ij}(t)$  and  $K_{ijk}(t)$  (Fig. 2(c)).

#### D. Reflecting and absorbing boundary conditions

We describe how to impose various boundary conditions on the formulations of the coarse-grained reaction dynamics. As will be shown in the next section, introducing boundary conditions is useful for applying the present method to the molecular binding processes through the returning probability theory.

We first consider the reflecting boundary condition, in which the population entering given states is instantly redirected to their neighboring states. Let  $\mathcal{M}_{\text{reflect}}$  be the set of states that prohibit such influx. The reflecting boundary condition can then be expressed as

$$\begin{aligned} \forall i \in \mathcal{M}_{\text{reflect}}, \forall j \in \mathcal{N}_i, \\ Q_{ji}(t) &= R_{ij}(t) \\ &+ \sum_{k \in \mathcal{N}_j} \int_0^t d\tau K_{ijk}(\tau) Q_{jk}(\tau), \end{aligned} \quad (40)$$

$$Q_{ij}(t) = 0, \quad (41)$$

for all such states.

Next, we consider the absorbing boundary condition, where a population that enters a particular state never exits to any other state again. Let  $\mathcal{M}_{\text{absorb}}$  denote the set of absorbing states. The absorbing boundary condition is then given by

$$\forall i \in \mathcal{M}_{\text{absorb}}, \forall j \in \mathcal{N}_i, \quad Q_{ji}(t) = 0, \quad (42)$$

which ensure the complete absence of influx from absorbing states.

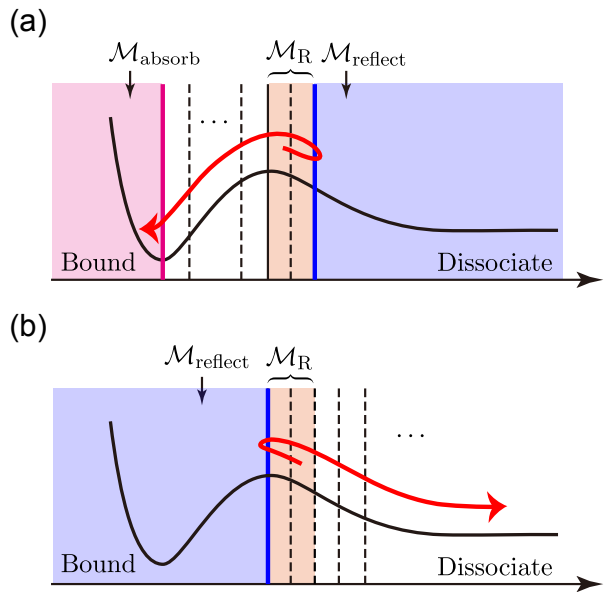


FIG. 3. Boundary conditions used for computing (a)  $k_{\text{ins}}$  and (b)  $P_{\text{RET}}(t)$ .  $\mathcal{M}_{\text{absorb}}$ ,  $\mathcal{M}_{\text{reflect}}$ , and  $\mathcal{M}_R$  denote the sets of absorbing, reflecting, and reactive states, respectively.

#### E. Incorporating returning probability (RP) theory

Returning-probability (RP) theory is a rigorous framework of diffusion-influenced reactions. In this approach, molecular binding is characterized in terms of the thermodynamic and dynamic properties of the reactive states that exists during the binding process. It has proven useful to analyze various systems including host-guest binding,<sup>44,45</sup> and membrane permeation.<sup>46</sup> In the case of binding, the reactive state is defined as the region near the barrier top on the free-energy profile separating the bound and unbound states, whereas in the case of membrane permeation, it corresponds to the membrane center. In this subsection, we describe the scheme of efficiently computing the dynamic properties required in the RP theory to evaluate the binding rate constant,  $k_{\text{on}}$ , based on the present theory.

The theoretical expression of  $k_{\text{on}}$  is given as

$$k_{\text{on}} = k_{\text{ins}} K^* \left( 1 + k_{\text{ins}} \int_0^\infty dt P_{\text{RET}}(t) \right)^{-1}, \quad (43)$$

where  $K^*$  is the equilibrium constant between the reactive and dissociate states.  $k_{\text{ins}}$  is the rate constant associated with the transition from the reactive state to the bound state.  $P_{\text{RET}}(t)$  is the returning probability, the conditional probability that the system is in the reactive states at time  $t$ , given that it was initially in the reactive states. The efficient calculation of  $K^*$  can be achieved using various free-energy calculation methods. Within the present framework, one can also efficiently calculate

$k_{\text{ins}}$  and  $P_{\text{RET}}(t)$  from short-timescale MD trajectories, provided that appropriate boundary conditions are imposed (Fig. 3). Let  $\mathcal{M}_R$  be the set of the reactive states, and set the initial states to be  $\mathcal{M}_R$  in calculations of both  $k_{\text{ins}}$  and  $P_{\text{RET}}(t)$ , i.e.,  $\mathcal{M}_I = \mathcal{M}_R$ . In the case of  $k_{\text{ins}}$ , the absorbing states ( $\mathcal{M}_{\text{absorb}}$ ) are introduced to define the completion of the binding process, whereas the reflecting states ( $\mathcal{M}_{\text{reflect}}$ ) are assigned to the specific neighboring states of the reactive states that lie on the dissociation side (Fig. 3(a)). Under this condition,  $k_{\text{ins}}$  can be expressed using  $P_j(t)$  as

$$\frac{1}{k_{\text{ins}}} = \int_0^\infty dt \sum_{j \notin \mathcal{M}_{\text{absorb}}} P_j(t). \quad (44)$$

Note that the right-hand side of the above equation is a theoretical expression of the mean first passage time (MFPT)<sup>50,54</sup> from the reactive state to the absorbing state corresponding to the well of the bound region in the free energy profile. For  $P_{\text{RET}}(t)$ , the neighboring states of the reactive states that lie on the bound-state side are designated as reflecting states (Fig. 3(b)). Then,  $P_{\text{RET}}(t)$  can be calculated as

$$P_{\text{RET}}(t) = \sum_{j \in \mathcal{M}_R} P_j(t). \quad (45)$$

It should be noted that the scheme for computing  $k_{\text{ins}}$  and  $P_{\text{RET}}(t)$  described above is also applicable to membrane permeation, where the insertion process corresponds to the transition of permeant molecules from the membrane center (reactive state) to the acceptor aqueous phase, and the returning process is the retention at or return to the membrane center for molecules initially located at the membrane center.

## F. Numerical implementation

In this subsection, we describe a scheme for computing  $P_{ij}(t)$  and  $Q_{ij}(t)$  from discretized time-series data.

Let the time interval of the time-series data be  $\Delta t$ , and denote the state of the system at time  $t = m\Delta t$  ( $m = 0, 1, \dots$ ) by  $W(m)$ . When the state of the system at time step  $m$  is  $j$ , the value of  $W(m)$  is set to  $j$ . To calculate  $R_{ij}(t)$ , time-series data satisfying  $W(0) = j$  are used. When the value of  $W(n)$  changes to  $i$  for the first time at time step  $n$ , this indicates that a transition to state  $i$  occurred within the interval  $(n-1)\Delta t \leq t < n\Delta t$ . If the system is in equilibrium at the initial time, the origin of time can be shifted so that this single transition event is regarded as having been observed immediately after time steps  $0, 1, \dots$ , and  $n-1$ . By constructing a histogram  $\tilde{R}_{ij}(m)$  for the time step immediately preceding the observation of a transition event,  $R_{ij}(t)$  can be calculated using the normalization condition

$$\sum_{l \in \mathcal{N}_j} \int_0^\infty dt R_{lj}(t) = w_j, \quad (46)$$

as

$$R_{ij}(m\Delta t) = \frac{w_j \tilde{R}_{ij}(m)}{\Delta t \sum_{l \in \mathcal{N}_j} \sum_{u=0}^\infty \tilde{R}_{lj}(u)}. \quad (47)$$

Here,  $w_j$  is the statistical weight of state  $j$ , as defined in Eq. (28). For  $K_{ijk}(t)$ , the value of  $W(0)$  in the time-series data can be arbitrary. Let  $n_1$  be the time step at which the transition from state  $k$  to  $j$  is observed for the first time; then  $n_1 - 1$  is set as the origin of time. If the transition to state  $i$  is next observed at time step  $n_2$ , the transition is considered to have occurred within the interval  $n_2 - n_1 - 1 \leq t/\Delta t < n_2 - n_1$ . Subsequently, by resetting the time origin to  $n_2 - 1$  and repeating the same procedure, a histogram  $\tilde{K}_{ijk}(m)$  can be constructed. Also, the number of observed transitions from state  $k$  to  $j$  is recorded as  $N_{jk}$ . Note that the last transition event in the time-series data is not counted to eliminate incomplete events. This restriction does not apply when state  $j$  is the outermost state that includes infinite separation to account for dissociation (i.e., no return to the outermost boundary). Then,  $K_{ijk}(m\Delta t)$  is calculated as

$$K_{ijk}(m\Delta t) = \frac{\tilde{K}_{ijk}(m)}{N_{jk}\Delta t}. \quad (48)$$

$P_j^0(t)$  and  $M_{ij}(m)$  can be computed from  $R_{ij}(m\Delta t)$  and  $K_{ijk}(t)$  based on Eqs. (38) and (39) as

$$P_j^0(m\Delta t) = w_j - \Delta t \sum_{n=0}^{m-1} \sum_{i \in \mathcal{N}_j} R_{ij}(n\Delta t), \quad (49)$$

$$M_{jk}(m\Delta t) = 1 - \Delta t \sum_{n=0}^{m-1} \sum_{i \in \mathcal{N}_j} K_{ijk}(n\Delta t), \quad (50)$$

respectively.

The governing equation for  $Q_{ij}(t)$  (Eq. (37)) can be written in a discretized form as

$$Q_{ij}(m\Delta t) = R_{ij}(m\Delta t) + \Delta t \sum_{k \in \mathcal{N}_j} \sum_{n=0}^{m-1} K_{ijk}((m-n)\Delta t) Q_{jk}(n\Delta t). \quad (51)$$

Since  $m = 0$  corresponds to  $Q_{ij}(0) = R_{ij}(0)$ ,  $Q_{ij}(m\Delta t)$  can be computed recursively, once  $R_{ij}(m\Delta t)$  and  $K_{ijk}(m\Delta t)$  have been evaluated up to a timescale at which these functions decay to zero. The discretized form of Eq. (32) is expressed as

$$P_j(m\Delta t) = P_j^0(m\Delta t) + \Delta t \sum_{k \in \mathcal{N}_j} \sum_{n=0}^{m-1} M_{jk}((m-n)\Delta t) Q_{jk}(n\Delta t), \quad (52)$$

and thus  $P_j(m\Delta t)$  can be computed from  $Q_{jk}(n\Delta t)$  for  $n < m$ .

### G. Analytical estimation of time constants

The kinetic parameters, such as  $k_{\text{ins}}$  (Eq. (44)), are related to the time integration of the population of state  $j$ , defined as

$$\tau_j = \int_0^\infty dt P_j(t), \quad (53)$$

in the presence of absorbing states or states that include infinite separation, which ensure that  $P_j(t)$  converges to zero in the limit  $t \rightarrow \infty$ . As described below, the time constants can be computed without computing the development of  $P_j(t)$  through Eqs. (51) and (52).

The Laplace transform of function  $f(t)$  is defined as

$$\tilde{f}(s) = \int_0^\infty dt e^{-st} f(t). \quad (54)$$

The Laplace transform of Eq. (32) is expressed as

$$\tilde{P}_j(s) = \tilde{P}_j^0(s) + \sum_{k \in \mathcal{N}_j} \tilde{M}_{jk}(s) \tilde{Q}_{jk}(s), \quad (55)$$

and taking the limit  $s \rightarrow 0$  leads to

$$\tau_j = \tilde{P}_j^0(0) + \sum_{k \in \mathcal{N}_j} \tilde{M}_{jk}(0) \tilde{Q}_{jk}(0). \quad (56)$$

$\tilde{P}_j^0(0)$ ,  $\tilde{M}_{jk}(0)$ , and  $\tilde{Q}_{jk}(0)$  are the time integrals of the corresponding time-dependent functions, and thus the remaining task is to evaluate  $\tilde{Q}_{jk}(0)$ . Let us introduce the following function:

$$\mathcal{K}_{ij,j'k}(t) = \delta_{jj'} K_{ijk}(t). \quad (57)$$

Here,  $\delta_{jj'}$  is Kronecker delta. Using  $\mathcal{K}_{ij,j'k}(t)$ , Eq. (37) can be rewritten as

$$\tilde{Q}_{ij}(s) = \tilde{R}_{ij}(s) + \sum_{j',k} \tilde{\mathcal{K}}_{ij,j'k}(s) \tilde{Q}_{j'k}(s). \quad (58)$$

Then, by denoting a pair of state indices (e.g.,  $ij$ ) by a single composite index  $\lambda, \mu, \dots$ , the above equation can be expressed in matrix form as  $\tilde{\mathbf{Q}}(s) = \tilde{\mathbf{R}}(s) + \tilde{\mathcal{K}}(s) \tilde{\mathbf{Q}}(s)$ , where  $\tilde{\mathbf{X}}(s)$  denotes a matrix whose  $(\lambda, \mu)$  element is  $\tilde{X}_{\lambda\mu}(s)$  when  $\tilde{\mathbf{X}}(s) = \tilde{\mathbf{K}}(s)$ , and a vector whose  $\lambda$ th element is  $\tilde{X}_\lambda(s)$  when  $\tilde{\mathbf{X}}(s) = \tilde{\mathbf{Q}}(s)$  or  $\tilde{\mathbf{R}}(s)$ . The solution of Eq. (58) in the limit  $s \rightarrow 0$  is given by

$$\tilde{\mathbf{Q}}(0) = [\mathbf{I} - \tilde{\mathcal{K}}(0)]^{-1} \tilde{\mathbf{R}}(0). \quad (59)$$

Here,  $\mathbf{I}$  is the identity matrix, and the  $(\lambda, \mu)$  element of  $\mathbf{I} - \tilde{\mathcal{K}}(0)$  is

$$(\mathbf{I} - \tilde{\mathcal{K}}(0))_{\lambda\mu} = \delta_{\lambda\mu} - \int_0^\infty dt \mathcal{K}_{\lambda\mu}(t), \quad (60)$$

and the  $\lambda$ th element of  $\tilde{\mathbf{R}}(0)$  is the time integral of  $R_\lambda(t)$ . Accordingly,  $\tilde{Q}_\lambda(0)$  can be evaluated using Eq. (59).

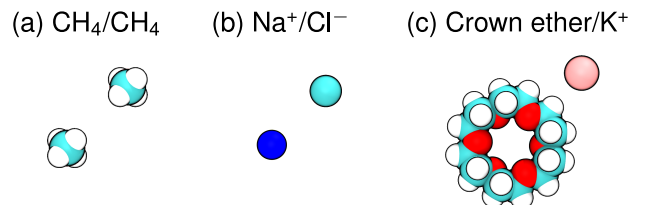


FIG. 4. Target binding/unbinding systems: (a)  $\text{CH}_4/\text{CH}_4$ , (b)  $\text{Na}^+/\text{Cl}^-$ , and (c) crown ether/ $\text{K}^+$ , each immersed in pure water. The molecular structures are visualized using Visual Molecular Dynamics (VMD) package.<sup>55</sup>

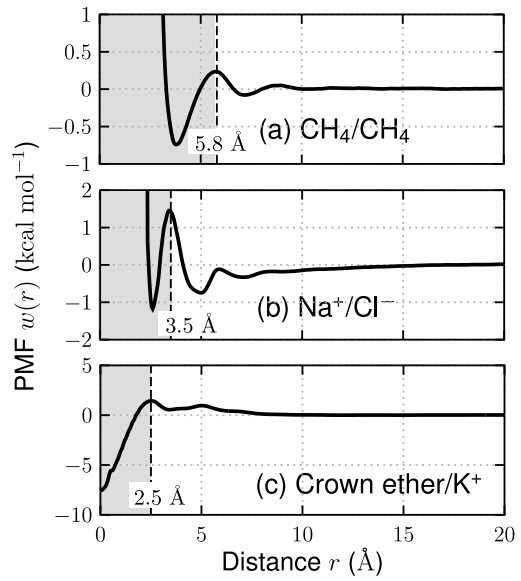


FIG. 5. Potentials of mean force (PMFs),  $w(r)$ , for (a)  $\text{CH}_4/\text{CH}_4$ , (b)  $\text{Na}^+/\text{Cl}^-$ , and (c) crown ether/ $\text{K}^+$ . Bound region (highlighted in gray) is defined by the barrier top position.

### III. COMPUTATIONAL DETAILS

We investigated three molecular binding/unbinding systems in water at 300 K and 1 atm:  $\text{CH}_4/\text{CH}_4$ ,  $\text{Na}^+/\text{Cl}^-$ , and 18-crown-6-ether (crown ether)/ $\text{K}^+$  (Fig. 4). The molecular models for each species are described in Sec. III A, while the simulation protocols are detailed in Secs. III B, III C, and III D. All analyses were performed using Analyze Trajectories (ANATRA) package developed by us (<https://github.com/kenkasa/anatra>).

The initial configurations of the systems were generated using Packmol.<sup>56</sup> All molecular dynamics (MD) simulations were performed using Amber 24.<sup>57-59</sup> The velocity Verlet integrator<sup>60</sup> was used with the time interval of 2 fs. The temperature and pressure were controlled using the Bussi thermostat<sup>61</sup> with the coupling time constant of 5 ps and the Monte Carlo barostat<sup>62</sup>, respectively.

TABLE I. The numbers of MD trajectories and trajectory length for each run used in the present method. The values in parentheses correspond to the case of binding kinetics. When values in parentheses are not shown, the listed values are common to both binding and unbinding cases.

$(N_B, \Delta_O)$		# of unbound states	# of traj.		Trajectory length (ns)		Total time ( $\mu$ s)
			Bound	Unbound	Bound	Unbound	
CH <sub>4</sub> /CH <sub>4</sub>	(1, 2 Å)	4	200	200	1	0.1	0.28
	(1, 3 Å)	3	200	200	1	0.1	0.26
	(3, 2 Å)	4	200	200	0.1	0.1	0.14
	(3, 3 Å)	3	200	200	0.1	0.1	0.12
Na <sup>+</sup> /Cl <sup>-</sup>	(1, 2 Å)	5	200	200	1	0.1	0.3
	(1, 3 Å)	4	200	200	1	0.1	0.28
	(3, 2 Å)	5	200	200	0.1	0.1	0.16
	(3, 3 Å)	4	200	200	0.1	0.1	0.14
Crown ether/K <sup>+</sup>	(3, 2 Å)	5	1000 (200)	200	2	1	7 (2.2)
	(3, 3 Å)	4	1000 (200)	200	2	1	6.8 (2.0)
	(3, 4 Å)	3	1000 (200)	200	2	1	6.6 (1.8)

TABLE II. The numbers of MD trajectories and trajectory length for each run for the brute-force MD simulations to evaluate the binding/unbinding kinetics.

	# of traj.		Trajectory length (ns)		Total time ( $\mu$ s)	
	Binding	Unbinding	Binding	Unbinding	Binding	Unbinding
CH <sub>4</sub> /CH <sub>4</sub>	100	200	10	1	1	0.2
Na <sup>+</sup> /Cl <sup>-</sup>	100	200	Avg. 27.4	1	2.74	0.2
Crown ether/K <sup>+</sup>	100	500	Avg. 208.6	Avg. 136.44	20.86	68.22

The Lennard-Jones interactions were truncated at 9 Å with long-range corrections applied.<sup>6</sup> Electrostatic interactions were computed using the smooth particle-mesh Ewald (SPME) method with 56 × 56 × 56 grid points. All the bonds involving hydrogen atoms were constrained by means of the SHAKE/RATTLE algorithms,<sup>63,64</sup> and the geometry of water molecules was kept rigid with the SETTLE algorithm.<sup>65</sup>

### A. Molecular models

The molecular structures of CH<sub>4</sub> and the crown ether were obtained by geometry optimization at the MP2/6-31G(d) level quantum mechanical (QM) calculations. The atomic point charges were then determined with the restrained electrostatic potential (RESP) method based on the HF/6-31G(d) level calculations. The QM calculations and the charge determination were performed using Gaussian 16<sup>66</sup> and Antechamber implemented in AmberTools,<sup>67</sup> respectively. The generalized Amber force field (GAFF)<sup>68,69</sup> was employed for CH<sub>4</sub> and the crown ether, while Joung-Cheatham model<sup>70</sup> and TIP3P<sup>71</sup> model were for ions (Na<sup>+</sup>, K<sup>+</sup>, and Cl<sup>-</sup>) and

water, respectively. For all the systems, the number of water molecules was set to 4000, and the simulation box size was 50<sup>3</sup> Å<sup>3</sup>.

### B. Umbrella sampling (US)

To evaluate the potentials of mean force (PMFs), we conducted the umbrella sampling (US) simulations.<sup>72,73</sup> The restraint potential was introduced to the distance of a pair of the target molecules,  $r$ , and was defined as  $U(r) = k(r - d)^2$ , where  $k$  and  $d$  respectively denote the force constant and reference distance. For CH<sub>4</sub> and the crown ether, the distance was defined using the carbon atom and the center of mass of the ether oxygen atoms, respectively. The force constant  $k$  was set to 10 kcal mol<sup>-1</sup> Å<sup>-2</sup> for all windows, and the spacing in  $d$  between adjacent windows was 0.1 Å. The lowest values of  $d$  were 3.3, 2.2, and 0 Å for the CH<sub>4</sub>/CH<sub>4</sub>, Na<sup>+</sup>/Cl<sup>-</sup>, and crown ether/K<sup>+</sup> systems, respectively, while the maximum value was set to 20 Å for all systems.

For each window, five initial configurations were prepared so that  $r$  was equal to the assigned value of  $d$ .

We performed a 1 ns *NVT* simulation, followed by a 1 ns *NPT* simulation for equilibration. Then, we conducted a *NPT* production simulation. The trajectory length of the production simulations was 3 ns for the  $\text{CH}_4/\text{CH}_4$  and  $\text{Na}^+/\text{Cl}^-$  systems and 5 ns for the crown ether/ $\text{K}^+$  system. The PMFs along the distance,  $w(r)$  (Fig. 5), were calculated using the multistate Bennett acceptance ratio (MBAR) method<sup>74</sup> implemented in GENESIS 2.1.<sup>75,76</sup>

### C. MD simulations for the present method

In order to calculate the quantities required for the present method ( $R_{ij}(t)$ ,  $K_{ijk}(t)$ ,  $P_j^0(t)$ , and  $M_{ij}(t)$ ), we performed a number of the short-timescale MD simulations starting from different states. To examine how the definition of states affects the binding/unbinding kinetics obtained using the present method, MD simulations corresponding to different sets of states were performed. Let  $N_B$  and  $\Delta_O$  denote the number of states belonging to the bound region (Fig. 5) and the width of the states outside the bound region (unbound states) in distance, respectively. The number of unbound states was determined such that the position of the outermost boundary separating adjacent states,  $d_{\text{OM}}$ , satisfied  $d_{\text{OM}} \geq 10 \text{ \AA}$ . An initial configuration was prepared for each state, in which the value of  $r$  lay within the range defined for that state. In the outermost state, the target molecules were placed so as to satisfy  $d_{\text{OM}} \leq r \leq d_{\text{OM}} + 2 \text{ \AA}$ .

For the  $\text{CH}_4/\text{CH}_4$  and  $\text{Na}^+/\text{Cl}^-$  systems, the examined combinations of  $(N_B, \Delta_O)$  were  $(1, 2 \text{ \AA})$ ,  $(1, 3 \text{ \AA})$ ,  $(3, 2 \text{ \AA})$ , and  $(3, 3 \text{ \AA})$ . For each state, 1 ns *NVT* and 1 ns *NPT* simulations with a flat-bottom restraint were performed sequentially for equilibration to keep the target molecules within the assigned state. The force constant of the flat-bottom restraint was  $10 \text{ kcal mol}^{-1} \text{ \AA}^{-2}$ . Subsequently, 200 trajectories were generated for each state using 0.1 ns *NPT* simulations with restraints and different random seeds, followed by 0.1 ns *NPT* simulations without restraints. For combinations with  $N_B = 1$ , the trajectory length for each bound state was extended to 1 ns. In the case of the crown ether/ $\text{K}^+$  system, the combinations  $(N_B, \Delta_O) = (3, 2 \text{ \AA})$ ,  $(3, 3 \text{ \AA})$ , and  $(3, 4 \text{ \AA})$  were examined. The simulation protocol was the same as that for the  $\text{CH}_4/\text{CH}_4$  and  $\text{Na}^+/\text{Cl}^-$  systems; however, the number of generated trajectories was set to 1000 for each bound state and 200 for each unbound state. The trajectory length of the production runs was set to 2 ns for each bound state and 1 ns for each unbound state. The numbers of production trajectories and the trajectory lengths for all systems are summarized in Table I. The time-series data of the distance were output every 20 fs.

To incorporate the present method with the returning probability theory (Eq. (43)), a reactive state was introduced. The unbound states (states outside the bound region) are divided into the reactive and dissociated states,

TABLE III. Residence time constants estimated from the present method and the brute-force MD simulations. For the present method, the time constants are evaluated under the condition  $(N_B, \Delta_O) = (3, 3 \text{ \AA})$ . The statistical uncertainty is provided at 95% confidence interval.

	$\tau_{\text{off}}$ (ns)	
	Present	Brute-force
$\text{CH}_4/\text{CH}_4$	$(1.8 \pm 0.1) \times 10^{-2}$	$(1.8 \pm 0.2) \times 10^{-2}$
$\text{Na}^+/\text{Cl}^-$	$(4.8 \pm 0.4) \times 10^{-2}$	$(3.9 \pm 0.5) \times 10^{-2}$
Crown ether/ $\text{K}^+$	$(1.0 \pm 0.2) \times 10^2$	$(1.1 \pm 0.1) \times 10^2$

as depicted schematically in Fig. 3. The barrier-top position was set as the lower bound of the state, and multiple values of the state width,  $\Delta R = 0.25, 0.50, 0.75, 1.00, 1.25, 1.50, 1.75$ , and  $2.00 \text{ \AA}$ , were examined. For each case, we conducted 200 *NPT* production simulations with a trajectory length of 0.1 ns, starting from the assigned reactive state.

### D. Brute-force MD simulations

We performed the brute-force MD simulations to evaluate the binding/unbinding kinetics for comparison with the results using the present method. The number of trajectories and trajectory length are described in Table II.

For the unbinding kinetics, initial configurations satisfying the binding criteria (gray-shaded regions in Fig. 5) were prepared, and equilibration runs were performed in the same manner as described in Sec. III C. In the cases of the  $\text{CH}_4/\text{CH}_4$  and  $\text{Na}^+/\text{Cl}^-$  systems, 1 ns *NPT* production simulation was performed for each run. As for the crown ether/ $\text{K}^+$  system, the trajectory length was extended in 10 ns increments until the distance between the target molecules,  $r$ , exceeded  $200 \text{ \AA}$  in the unwrapped trajectories.

Regarding the binding kinetics, the initial configurations were constructed without any restriction to the positions of the target molecules. After equilibration, as in the other types of simulations, *NPT* simulations were performed in 10 ns increments until the distance  $r$  became smaller than a predefined threshold. The threshold was set to the most stable separation for the  $\text{CH}_4/\text{CH}_4$  and  $\text{Na}^+/\text{Cl}^-$  systems, and to  $0.3 \text{ \AA}$  for the crown ether/ $\text{K}^+$  system (Fig. 5).

## IV. RESULTS AND DISCUSSION

### A. Unbinding kinetics

We first examine the reliability of the present method in terms of the unbinding kinetics. The residence time

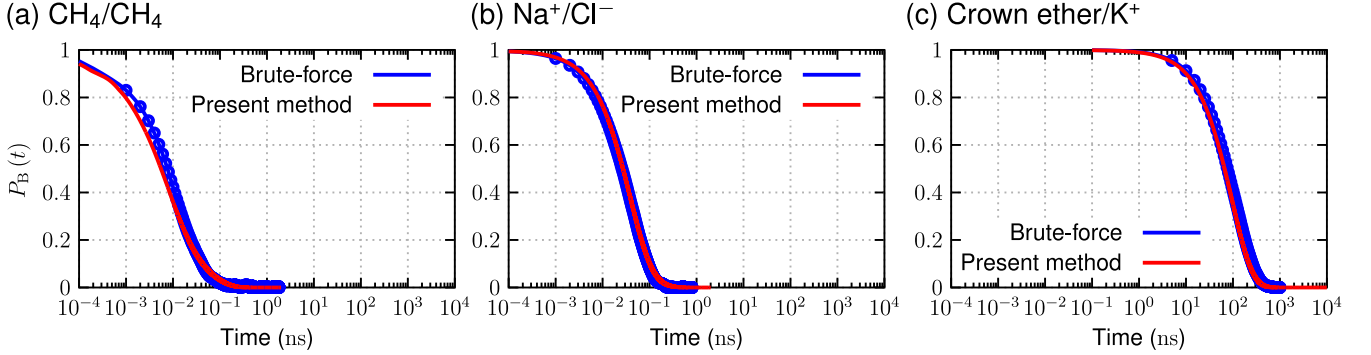


FIG. 6. Residence time correlation function,  $P_B(t)$ , for (a)  $\text{CH}_4/\text{CH}_4$ , (b)  $\text{Na}^+/\text{Cl}^-$ , and (c) crown ether/ $\text{K}^+$ . For the present method, the results obtained under the condition  $(N_B, \Delta_O) = (3, 3 \text{ \AA})$  are shown, where  $N_B$  and  $\Delta_O$  are the number of divisions for the bound region (Fig. 5) and the width of the states outside the bound region, respectively.

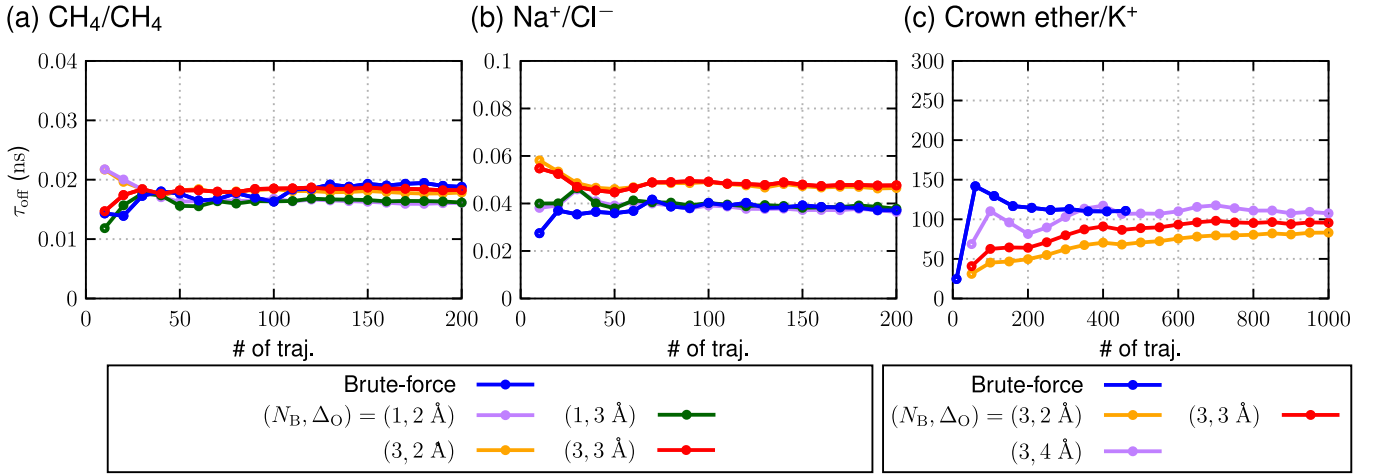


FIG. 7. Statistical convergence of  $\tau_{\text{off}}$  with respect to the number of trajectories, for (a)  $\text{CH}_4/\text{CH}_4$ , (b)  $\text{Na}^+/\text{Cl}^-$ , and (c) crown ether/ $\text{K}^+$ . For the crown ether/ $\text{K}^+$  system, the number of trajectories corresponding to the states outside the bound region (unbound states) is fixed to 200, because the value of  $\tau_{\text{off}}$  is found to be less sensitive to the number of trajectories in the unbound states as compared to those in the bound region.

correlation function,  $P_B(t)$ , defined as

$$P_B(t) = \sum_{j \in \mathcal{M}_B} P_j(t), \quad (61)$$

where  $\mathcal{M}_B$  is the set of the bound states. In the computation of  $P_B(t)$ , the initial condition is set using the characteristic function (Eq. (2)) as

$$P_j(0) = \begin{cases} \frac{\langle \Theta_j(\zeta) \rangle}{\sum_{k \in \mathcal{M}_B} \langle \Theta_k(\zeta) \rangle} & \text{for } j \in \mathcal{M}_R \\ 0 & \text{for } j \notin \mathcal{M}_B \end{cases}. \quad (62)$$

Fig. 6 shows  $P_B(t)$  computed using the present method under the condition  $(N_B, \Delta_O) = (3, 3 \text{ \AA})$ , together with the corresponding results obtained from the brute-force MD simulations. Here,  $N_B$  and  $\Delta_O$  respectively denote the number of division of the bound region and the distance width of the states outside the bound region. The

time interval used for discretization,  $\Delta t$  (see Sec. II F), is set to 20 fs for the  $\text{CH}_4/\text{CH}_4$  and  $\text{Na}^+/\text{Cl}^-$  systems and to 60 fs for the crown ether/ $\text{K}^+$  system. As shown in Fig. 6, the present method reproduces the profiles of  $P_B(t)$  obtained from the brute-force MD simulations well, although a difference is slightly discernible for the  $\text{CH}_4/\text{CH}_4$  system at  $t \leq 10^{-2}$  ns.  $P_B(t)$  converges to zero on the timescale of  $10^{-2}$ – $10^{-1}$  ns for both the  $\text{CH}_4/\text{CH}_4$  and  $\text{Na}^+/\text{Cl}^-$  systems, and this timescale is comparable to that obtained from the brute-force MD simulations (0.2 ns). In the case of the crown ether/ $\text{K}^+$  system, on the other hand, it is noteworthy that the present method enables the estimation of the timescale on which  $P_B(t)$  converges to zero ( $10^2$ – $10^3$  ns) from a number of short-timescale (2 ns) trajectories.

We next investigate the dependency of the unbinding kinetics obtained from the present method on the combinations of  $(N_B, \Delta_O)$  and the number of trajectories. In this analysis, the dependency is evaluated with the un-

TABLE IV. Binding rate constants,  $k_{\text{on}}$ , obtained from the present method and brute-force MD simulations. For the present method, the values of  $k_{\text{on}}$  are computed under the conditions  $(N_B, \Delta_O) = (3, 3 \text{ \AA})$  and  $\Delta R = 1 \text{ \AA}$ . The statistical uncertainty is provided at 95% confidence interval.

$k_{\text{on}} (\text{s}^{-1} \text{ M}^{-1})$		
	Present	Brute-force
$\text{CH}_4/\text{CH}_4$	$(3.4 \pm 0.2) \times 10^{10}$	$(3.2 \pm 0.6) \times 10^{10}$
$\text{Na}^+/\text{Cl}^-$	$(4.4 \pm 0.7) \times 10^9$	$(3.3 \pm 0.6) \times 10^9$
Crown ether/ $\text{K}^+$	$(4 \pm 1) \times 10^8$	$(3.6 \pm 0.6) \times 10^8$

binding time constant,  $\tau_{\text{off}}$ , defined as

$$\tau_{\text{off}} = \int_0^\infty dt P_B(t). \quad (63)$$

The values of  $\tau_{\text{off}}$  under the condition  $(N_B, \Delta_O) = (3, 3 \text{ \AA})$  are listed in Table III. Figure 7 illustrates how  $\tau_{\text{off}}$  depends on the number of trajectories,  $N_{\text{traj}}$ , for different combinations of  $(N_B, \Delta_O)$ .  $N_{\text{traj}}$  denotes the number of trajectories per state used in the present method and the number of trajectories starting from the bound region in the brute-force MD simulations. In the case of the crown ether/ $\text{K}^+$  (Fig. 7(c)), the number of trajectories for the states outside the bound region is fixed to 200. For the  $\text{CH}_4/\text{CH}_4$  system (Fig. 7(a)), the convergence of  $\tau_{\text{off}}$  is achieved when  $N_{\text{traj}}$  is larger than approximately 70, regardless of the choice of  $(N_B, \Delta_O)$ . It is also found that the converged value of  $\tau_{\text{off}}$  is almost independent of  $(N_B, \Delta_O)$ . The converged value is larger than that obtained from the brute-force MD simulations, but the deviation is below 10%. As for the  $\text{Na}^+/\text{Cl}^-$  system, the convergence is observed when  $N_{\text{traj}} \gtrsim 70$  for both the present method and the brute-force MD simulations. The  $N_B$ -dependence is slightly discernible, and the converged values of  $\tau_{\text{off}}$  at  $N_B = 1$  are virtually identical to that for the brute-force MD simulations. The quantitative improvement with decreasing  $N_B$  is a reasonable trend, as the approximation introduced in the present method (Eqs. (32) and (37)) is expected to be valid when the spacing between adjacent states is sufficiently large. In the case of the crown ether/ $\text{K}^+$  system, convergence with respect to  $N_{\text{traj}}$  is slower compared with the other systems, especially for  $(N_B, \Delta_O) = (3, 2 \text{ \AA})$ . Although the  $\Delta_O$ -dependence is also observed, the difference in the converged values between  $(3, 3 \text{ \AA})$  and  $(3, 4 \text{ \AA})$  is negligibly small, and these values are satisfactorily close to that obtained from the brute-force MD simulations.

## B. Binding kinetics

In this subsection, we discuss the application of the present method to molecular binding in the  $\text{CH}_4/\text{CH}_4$ ,  $\text{Na}^+/\text{Cl}^-$ , and crown ether/ $\text{K}^+$  systems through the returning probability theory (Sec. II E).  $P_{\text{RET}}(t)$  and

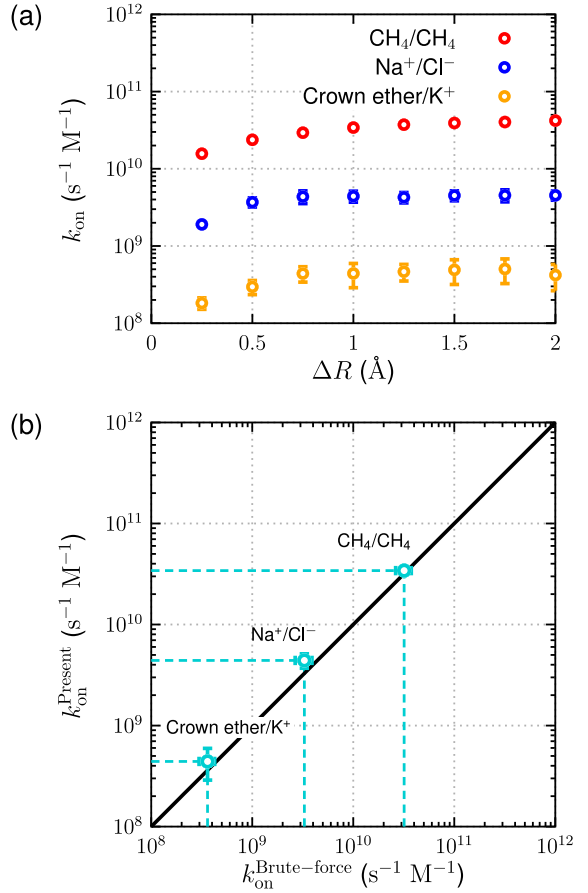


FIG. 8. Binding rate constants,  $k_{\text{on}}$ . (a) Dependency of  $k_{\text{on}}$  on the choice of the width of the reactive state,  $\Delta R$ . (b) Comparison of  $k_{\text{on}}$  between the present method ( $k_{\text{on}}^{\text{Present}}$ ) and the brute-force MD simulations ( $k_{\text{on}}^{\text{Brute-force}}$ ). For both figures, the present method is applied under the condition  $(N_B, \Delta_O) = (3, 3 \text{ \AA})$ , and  $\Delta R$  is set to  $1 \text{ \AA}$  for (b). The statistical uncertainty is provided at 95% confidence interval.

$k_{\text{ins}}$  involved in Eq. (43) are computed from the present method under the corresponding absorbing and reflecting boundary conditions. The value of  $K^*$  is calculated based on the population ratio of the reactive state relative to an arbitrarily chosen unbound region including the standard state correction,<sup>44,77</sup> with the US trajectories. For all cases, the state definition is based on the combination  $(N_B, \Delta_O) = (3, 3 \text{ \AA})$ , with a reactive state of width  $\Delta R$ . The lower bound of the reactive state corresponds to the boundary separating the bound region from the other regions, as described in the last paragraph of Sec. III C. In the previous studies on protein-ligand binding<sup>45</sup> and membrane permeation<sup>46</sup>, the appropriate width of the reactive state was determined such that the kinetic constants of interest are insensitive to the variation in the width.

The  $\Delta R$ -dependence of  $k_{\text{on}}$  is depicted in Fig. 8(a). For all systems, while  $k_{\text{on}}$  exhibits a dependence on  $\Delta R$  when  $\Delta R \leq 0.75 \text{ \AA}$ , the profile of  $k_{\text{on}}$  along  $\Delta R$  is almost flat

within the range of  $1 \leq \Delta R/\text{\AA} < 2$ . A similar trend has been observed for the protein-ligand binding<sup>45</sup>, where the definition dependence of  $k_{\text{on}}$  becomes noticeable when the reactive state is defined too narrowly. In the present study, we set  $\Delta R$  to 1 Å in the subsequent analysis.

Fig. 8(b) shows the comparison of  $k_{\text{on}}$  between the present method and brute-force MD simulations. The values of  $k_{\text{on}}$  are also listed in Table IV. The present method estimates that  $k_{\text{on}}$  increases in the order of  $\text{CH}_4/\text{CH}_4 > \text{Na}^+/\text{Cl}^- > \text{crown ether}/\text{K}^+$ . This ordering is consistent with that predicted from the brute-force MD simulations. Moreover, for all systems, the deviation of  $k_{\text{on}}$  from the values obtained by brute-force MD simulations is within  $\sim 40\%$ , indicating that the present method is useful for semi-quantitative ranking of binding kinetics with reduced computational cost compared to the brute-force approach.

## V. CONCLUSION

In this study, a new method was developed to describe the time evolution of the populations of distinct states in a system of interest by means of molecular dynamics (MD) simulations. Based on mathematical techniques developed in the field of diffusion-influenced reaction theory, a Liouville equation for the probability density of each state was derived, in which the influx from and efflux to neighboring states are explicitly incorporated. Subsequently, a Markov approximation for the processes of crossing the boundaries separating the states was introduced, resulting in a tractable set of integral equations that describe the population of each state. Since the time-dependent quantities involved in the derived equations for a given state are connected to only a few states near the state, these quantities can be evaluated through the short-timescale MD simulations. We also presented a scheme for introducing absorbing and reflecting boundaries, making the method compatible with the returning probability theory for evaluating binding rate constants.

The present method was applied to the binding and unbinding of the  $\text{CH}_4/\text{CH}_4$ ,  $\text{Na}^+/\text{Cl}^-$ , and 18-crown-6-ether (crown ether)/ $\text{K}^+$  in water. For the unbinding processes, the time constants,  $\tau_{\text{off}}$ , obtained from the present method were satisfactorily close to those from the brute-force MD simulations, with deviations of less than approximately 10%. Remarkably, for the crown ether/ $\text{K}^+$  system, the present method reproduced an unbinding timescale exceeding  $10^2$  ns from a number of short-timescale (1–2 ns) simulations. Regarding the binding kinetics, the ordering of binding rate constants,  $k_{\text{on}}$ , predicted from the present method was the same as that from the brute-force MD simulations. Furthermore, the deviation of  $k_{\text{on}}$  from the values obtained by the brute-force MD simulations was within  $\sim 40\%$ , enabling semi-quantitative ranking of the binding kinetics using MD simulations with timescales much shorter than those required for the brute-force MD approach.

As demonstrated by the applications in the present study, the present method allows reliable estimation of the rate constants for binding and unbinding kinetics from the short-timescale MD simulations. Thus, complex protein–ligand binding systems, such as trypsin/benzamidine, Janus kinase (JAK)/inhibitors, threonine–tyrosine kinase (TTK)/inhibitors, and heat shock protein 90 (Hsp90)/inhibitors, for which the binding and unbinding rate constants have been experimentally measured,<sup>78</sup> are potential targets of the present method for elucidating the underlying binding mechanisms with quantitative assessment. To further expand the applicability of the present method, on the other hand, reducing the number of required trajectories is important. In the Markovian milestone with Voronoi tessellations (MMVT) method,<sup>29</sup> the efficiency of sampling transition events is improved by introducing reflecting boundaries between states into MD simulations. Incorporating such simulation techniques could help reduce the computational cost of the present method. We anticipate that the present method and its extensions will be useful for unveiling the mechanisms underlying a variety of molecular kinetic processes in complex systems.

## ACKNOWLEDGMENTS

This work is supported by the Grants-in-Aid for Scientific Research (Grant Nos. JP21H05249, JP23K26617, JP23K27313, JP23K23303, JP23KK0254, JP24K21756, JP25H02464, and JP25K02235) from the Japan Society for the Promotion of Science, the Fugaku Supercomputer Project (Nos. JPMXP1020230325 and JPMXP1020230327) and the Data-Driven Material Research Project (No. JPMXP1122714694) from the Ministry of Education, Culture, Sports, Science, and Technology, the Core Research for Evolutional Science and Technology (CREST) from Japan Science and Technology Agency (JST) (No. JPMJCR22E3), and by Maruho Collaborative Project for Theoretical Pharmaceuticals. The simulations were conducted using Genkai A at Kyushu University, Fugaku at RIKEN Center for Computational Science through the HPCI System Research Project, and the supercomputer at the Research Center for Computational Sciences in Okazaki (Project IDs: hp250115, hp250211, hp250227, hp250229, 24-IMS-C105, and 25-IMS-C052).

## CONFLICT OF INTEREST

The authors have no conflicts to disclose.

## DATA AVAILABILITY

The data that support the findings of this study are available from the corresponding authors upon reason-

able request.

## Appendix A: Derivation of Eqs. (38) and (39)

In this appendix, we describe the relationship between  $P_j^0(t)$  (Eq. (27)) and  $R_{ij}(t)$  (Eq. (34)) and that between  $M_{ij}(t)$  (Eq. (31)) and  $K_{ijk}(t)$  (Eq. (36)).

From the definition of  $\mathcal{L}_j$  (Eq. (19)) and the relationship given by  $d\mathcal{L}_j e^{-\mathcal{L}_j t}/dt = -\mathcal{L}_j e^{-\mathcal{L}_j t}$ , the time derivative of  $P_j^0(t)$  (Eq. (27)) is expressed as

$$\begin{aligned} \frac{d}{dt} P_j^0(t) &= \frac{d}{dt} \left\langle \left\langle e^{-\mathcal{L}_j t} \hat{f}_j(\boldsymbol{\Gamma}, 0) \right\rangle \right\rangle_I \\ &= - \sum_{i \in \mathcal{N}_j} \left\langle \left\langle S_{ij}(\boldsymbol{\zeta}, \dot{\boldsymbol{\zeta}}) e^{-\mathcal{L}_j t} \hat{f}_j(\boldsymbol{\Gamma}, 0) \right\rangle \right\rangle_I \\ &\quad + \frac{d}{dt} \left[ P_j^0(t) \right]_{\text{NR}}, \end{aligned} \quad (\text{A1})$$

where

$$\frac{d}{dt} \left[ P_j^0(t) \right]_{\text{NR}} = - \left\langle \left\langle \mathcal{L} \left[ e^{-\mathcal{L}_j t} \hat{f}_j(\boldsymbol{\Gamma}, 0) \right] \right\rangle \right\rangle_I. \quad (\text{A2})$$

$d[\dots]_{\text{NR}}/dt$  represents the time derivative without reaction (efflux and influx), governed by the Liouville operator  $\mathcal{L}$ . Given that the population is conserved in the dynamics described by  $\mathcal{L}$ ,  $d[P_j^0(t)]_{\text{NR}}/dt$  vanishes. Furthermore, Eq. (A1) can be rewritten from the definition of  $R_{ij}^0(t)$  (Eq. (34)) as

$$\frac{d}{dt} P_j^0(t) = - \sum_{i \in \mathcal{N}_j} R_{ij}(t), \quad (\text{A3})$$

and its time integral gives

$$P_j^0(t) = P_j^0(0) - \sum_{i \in \mathcal{N}_j} \int_0^t d\tau R_{ij}(\tau). \quad (\text{A4})$$

Since  $P_j^0(0)$  is  $w_j$  (Eq. (28)), the above equation is equivalent to Eq. (38).

The relationship between  $M_{ij}(t)$  and  $K_{ijk}(t)$  (Eq. (39)) can be derived in a similar way. From Eqs. (19), (31), and (36), one can obtain

$$\frac{d}{dt} M_{jk}(t) = - \sum_{i \in \mathcal{N}_j} K_{ijk}(t) + \frac{d}{dt} \left[ M_{jk}(t) \right]_{\text{NR}}, \quad (\text{A5})$$

and the second term on the right-hand side vanishes due to the conservation of population. Since the initial value of  $M_{ij}(t)$  is unity, the time integral of the above equation yields

$$M_{jk}(t) = 1 - \sum_{i \in \mathcal{N}_j} \int_0^t d\tau K_{ijk}(\tau). \quad (\text{A6})$$

<sup>1</sup>B. Schuler and H. Hofmann, “Single-molecule spectroscopy of protein folding dynamics—expanding scope and timescales,” *Curr. Opin. Struct. Biol.* **23**, 36–47 (2013).

<sup>2</sup>H. S. Chung, K. McHale, J. M. Louis, and W. A. Eaton, “Single-molecule fluorescence experiments determine protein folding transition path times,” *Science* **335**, 981–984 (2012).

<sup>3</sup>R. L. Rich and D. G. Myszka, “Advances in surface plasmon resonance biosensor analysis,” *Curr. Opin. Biotechnol.* **11**, 54–61 (2000).

<sup>4</sup>P. Pattnaik, “Surface plasmon resonance: applications in understanding receptor-ligand interaction,” *Appl. Biochem. Biotechnol.* **126**, 79–92 (2005).

<sup>5</sup>S. G. Patching, “Surface plasmon resonance spectroscopy for characterisation of membrane protein–ligand interactions and its potential for drug discovery,” *Biochim. Biophys. Acta - Biomembr.* **1838**, 43–55 (2014).

<sup>6</sup>M. P. Allen and D. J. Tildesley, *Computer simulation of liquids* (Oxford university press, 2017).

<sup>7</sup>D. Frenkel and B. Smit, *Understanding molecular simulation: from algorithms to applications*, Vol. 1 (Elsevier, 2001).

<sup>8</sup>M. Bonomi and C. Camilloni, “Biomolecular simulations,” *Methods in Molecular Biology* **2022** (2019).

<sup>9</sup>F. Sohraby and A. Nunes-Alves, “Advances in computational methods for ligand binding kinetics,” *Trends Biochem. Sci.* **48**, 437–449 (2023).

<sup>10</sup>V. S. Pande, K. Beauchamp, and G. R. Bowman, “Everything you wanted to know about markov state models but were afraid to ask,” *Methods* **52**, 99–105 (2010).

<sup>11</sup>G. R. Bowman, V. S. Pande, and F. Noé, *An introduction to Markov state models and their application to long timescale molecular simulation*, Vol. 797 (Springer Science & Business Media, 2013).

<sup>12</sup>J. D. Chodera and F. Noé, “Markov state models of biomolecular conformational dynamics,” *Curr. Opin. Struct. Biol.* **25**, 135–144 (2014).

<sup>13</sup>P. Tiwary, V. Limongelli, M. Salvalaglio, and M. Parrinello, “Kinetics of protein–ligand unbinding: Predicting pathways, rates, and rate-limiting steps,” *Proc. Natl. Acad. Sci.* **112**, E386–E391 (2015).

<sup>14</sup>H. Wu, F. Paul, C. Wehmeyer, and F. Noé, “Multiensemble markov models of molecular thermodynamics and kinetics,” *Proc. Natl. Acad. Sci.* **113**, E3221–E3230 (2016).

<sup>15</sup>S. D. Lotz and A. Dickson, “Unbiased molecular dynamics of 11 min timescale drug unbinding reveals transition state stabilizing interactions,” *J. Am. Chem. Soc.* **140**, 618–628 (2018).

<sup>16</sup>R. Harada and Y. Shigeta, “Hybrid cascade-type molecular dynamics with a markov state model for efficient free energy calculations,” *J. Chem. Theory Comput.* **15**, 680–687 (2018).

<sup>17</sup>D. P. Tran and A. Kitao, “Dissociation process of MDM2/p53 complex investigated by parallel cascade selection molecular dynamics and markov state model,” *J. Phys. Chem. B* (2019).

<sup>18</sup>R. T. McGibbon and V. S. Pande, “Variational cross-validation of slow dynamical modes in molecular kinetics,” *J. Chem. Phys.* **142** (2015).

<sup>19</sup>A. Mardt, L. Pasquali, H. Wu, and F. Noé, “VAMPnets for deep learning of molecular kinetics,” *Nat. Commun.* **9**, 5 (2018).

<sup>20</sup>H. Wu and F. Noé, “Variational approach for learning markov processes from time series data,” *J. Nonlinear Sci.* **30**, 23–66 (2020).

<sup>21</sup>E. Suárez, R. P. Wiewiora, C. Wehmeyer, F. Noé, J. D. Chodera, and D. M. Zuckerman, “What markov state models can and cannot do: Correlation versus path-based observables in protein-folding models,” *J. Chem. Theory Comput.* **17**, 3119–3133 (2021).

<sup>22</sup>E. Suárez, S. Lettieri, M. C. Zwier, S. R. Subramanian, L. T. Chong, and D. M. Zuckerman, “Simultaneous computation of dynamical and equilibrium information using a weighted ensemble of trajectories,” *Biophys. J.* **106**, 406a (2014).

<sup>23</sup>E. Suárez, J. L. Adelman, and D. M. Zuckerman, “Accurate estimation of protein folding and unfolding times: beyond markov

state models,” *J. Chem. Theory Comput.* **12**, 3473–3481 (2016).

<sup>24</sup>S. Cao, A. Montoya-Castillo, W. Wang, T. E. Markland, and X. Huang, “On the advantages of exploiting memory in markov state models for biomolecular dynamics,” *J. Chem. Phys.* **153**, 014105 (2020).

<sup>25</sup>S. Cao, Y. Qiu, M. L. Kalin, and X. Huang, “Integrative generalized master equation: A method to study long-timescale biomolecular dynamics via the integrals of memory kernels,” *J. Chem. Phys.* **159** (2023).

<sup>26</sup>R. Elber, “Milestoning: An efficient approach for atomically detailed simulations of kinetics in biophysics,” *Annu. Rev. Biophys.* **49**, 69–85 (2020).

<sup>27</sup>A. K. Faradjian and R. Elber, “Computing time scales from reaction coordinates by milestoning,” *J. Chem. Phys.* **120**, 10880–10889 (2004).

<sup>28</sup>E. Vanden-Eijnden, M. Venturoli, G. Ciccotti, and R. Elber, “On the assumptions underlying milestoning,” *J. Chem. Phys.* **129**, 174102 (2008).

<sup>29</sup>E. Vanden-Eijnden and M. Venturoli, “Markovian milestoning with voronoi tessellations,” *The Journal of chemical physics* **130**, 194101 (2009).

<sup>30</sup>D. Ray and I. Andricioaei, “Weighted ensemble milestoning (WEM): A combined approach for rare event simulations,” *J. Chem. Phys.* **152** (2020).

<sup>31</sup>D. Ray, S. E. Stone, and I. Andricioaei, “Markovian weighted ensemble milestoning (M-WEM): Long-time kinetics from short trajectories,” *J. Chem. Theory Comput.* **18**, 79–95 (2021).

<sup>32</sup>L. W. Votapka, B. R. Jagger, A. L. Heyneman, and R. E. Amaro, “Seekr: Simulation enabled estimation of kinetic rates, a computational tool to estimate molecular kinetics and its application to trypsin–benzamidine binding,” *J. Phys. Chem. B* **121**, 3597–3606 (2017).

<sup>33</sup>L. W. Votapka, A. M. Stokely, A. A. Ojha, and R. E. Amaro, “Seekr2: Versatile multiscale milestoning utilizing the openmm molecular dynamics engine,” *J. Chem. Inf. Model.* **62**, 3253–3262 (2022).

<sup>34</sup>T. Ruzmetov, R. Montes, J. Sun, S.-H. Chen, Z. Tang, and C.-e. A. Chang, “Binding kinetics toolkit for analyzing transient molecular conformations and computing free energy landscapes,” *J. Phys. Chem. A* **126**, 8761–8770 (2022).

<sup>35</sup>G. A. Huber and S. Kim, “Weighted-ensemble brownian dynamics simulations for protein association reactions,” *Biophys. J.* **70**, 97–110 (1996).

<sup>36</sup>D. M. Zuckerman and L. T. Chong, “Weighted ensemble simulation: review of methodology, applications, and software,” *Annu. Rev. Biophys.* **46**, 43–57 (2017).

<sup>37</sup>D. Aristoff, J. Copperman, G. Simpson, R. J. Webber, and D. M. Zuckerman, “Weighted ensemble: Recent mathematical developments,” *J. Chem. Phys.* **158**, 014108 (2023).

<sup>38</sup>S. A. Rice, *Diffusion-limited reactions*, Vol. 25 (Elsevier, 1985).

<sup>39</sup>K. Kasahara and H. Sato, “Dynamics theory for molecular liquids based on an interaction site model,” *Phys. Chem. Chem. Phys.* **19**, 27917–27929 (2017).

<sup>40</sup>K. Lindenberg, R. Metzler, and G. Oshanin, *Chemical Kinetics: beyond the textbook* (World scientific, 2019).

<sup>41</sup>G. Wilemski and M. Fixman, “General theory of diffusion-controlled reactions,” *J. Chem. Phys.* **58**, 4009–4019 (1973).

<sup>42</sup>G. H. Weiss, “A perturbation analysis of the wilemski–fixman approximation for diffusion-controlled reactions,” *J. Chem. Phys.* **80**, 2880–2887 (1984).

<sup>43</sup>J.-H. Kim and S. Lee, “A rigorous foundation of the diffusion-influenced bimolecular reaction kinetics,” *J. Chem. Phys.* **131**, 014503 (2009).

<sup>44</sup>K. Kasahara, R. Masayama, K. Okita, and N. Matubayasi, “Atomistic description of molecular binding processes based on returning probability theory,” *J. Chem. Phys.* **155**, 204503 (2021).

<sup>45</sup>K. Kasahara, R. Masayama, K. Okita, and N. Matubayasi, “Elucidating protein–ligand binding kinetics based on returning probability theory,” *J. Chem. Phys.* **159**, 134103 (2023).

<sup>46</sup>Y. Matsubara, R. Okabe, R. Masayama, N. Watanabe, Morishita, H. Umakoshi, K. Kasahara, and N. Matubayasi, “A methodology of quantifying membrane permeability based on returning probability theory and molecular dynamics simulation,” *J. Chem. Phys.* **161**, 024108 (2024).

<sup>47</sup>J. M. Bello-Rivas and R. Elber, “Exact milestoning,” *J. Chem. Phys.* **142** (2015).

<sup>48</sup>A. Luzar and D. Chandler, “Hydrogen-bond kinetics in liquid water,” *Nature* **379**, 55–57 (1996).

<sup>49</sup>D. Laage and J. T. Hynes, “A molecular jump mechanism of water reorientation,” *Science* **311**, 832–835 (2006).

<sup>50</sup>N. G. Van Kampen, *Stochastic processes in physics and chemistry*, Vol. 1 (Elsevier, 1992).

<sup>51</sup>S. G. Kou and H. Wang, “First passage times of a jump diffusion process,” *Adv. Appl. Probab.* **35**, 504–531 (2003).

<sup>52</sup>M. C. Zwier, J. W. Kaus, and L. T. Chong, “Efficient explicit-solvent molecular dynamics simulations of molecular association kinetics: Methane/methane,  $\text{Na}^+/\text{Cl}^-$ , methane/benzene, and  $\text{K}^+/\text{18-crown-6}$  ether,” *J. Chem. Theory Comput.* **7**, 1189–1197 (2011).

<sup>53</sup>A. Molski, “A source term formalism for the reactive Fokker-Planck dynamics,” *Chem. Phys. Lett.* **148**, 562–566 (1988).

<sup>54</sup>N. F. Polizzi, M. J. Therien, and D. N. Beratan, “Mean first-passage times in biology,” *Isr. J. Chem.* **56**, 816–824 (2016).

<sup>55</sup>W. Humphrey, A. Dalke, and K. Schulten, “VMD: visual molecular dynamics,” *J. Mol. Graph.* **14**, 33–38 (1996).

<sup>56</sup>L. Martínez, R. Andrade, E. G. Birgin, and J. M. Martínez, “PACKMOL: a package for building initial configurations for molecular dynamics simulations,” *J. Comput. Chem.* **30**, 2157–2164 (2009).

<sup>57</sup>D. A. Case, D. S. Cerutti, V. W. D. Cruzeiro, T. A. Darden, R. E. Duke, M. Ghazimirsaeed, G. M. Giambasut, T. J. Giese, A. W. Gotz, J. A. Harris, *et al.*, “Recent developments in amber biomolecular simulations,” *J. Chem. Inf. Model.* **65**, 7835–7843 (2025).

<sup>58</sup>R. Salomon-Ferrer, A. W. Gotz, D. Poole, S. Le Grand, and R. C. Walker, “Routine microsecond molecular dynamics simulations with amber on gpus. 2. explicit solvent particle mesh ewald,” *J. Chem. Theory Comput.* **9**, 3878–3888 (2013).

<sup>59</sup>S. Le Grand, A. W. Götz, and R. C. Walker, “SPFP: Speed without compromise—a mixed precision model for gpu accelerated molecular dynamics simulations,” *Comput. Phys. Commun.* **184**, 374–380 (2013).

<sup>60</sup>W. C. Swope, H. C. Andersen, P. H. Berens, and K. R. Wilson, “A computer simulation method for the calculation of equilibrium constants for the formation of physical clusters of molecules: Application to small water clusters,” *J. Chem. Phys.* **76**, 637–649 (1982).

<sup>61</sup>G. Bussi, D. Donadio, and M. Parrinello, “Canonical sampling through velocity rescaling,” *J. Chem. Phys.* **126**, 014101 (2007).

<sup>62</sup>J. Åqvist, P. Wennerström, M. Nervall, S. Bjelic, and B. O. Brandsdal, “Molecular dynamics simulations of water and biomolecules with a monte carlo constant pressure algorithm,” *Chem. Phys. Lett.* **384**, 288–294 (2004).

<sup>63</sup>J.-P. Ryckaert, G. Ciccotti, and H. J. Berendsen, “Numerical integration of the cartesian equations of motion of a system with constraints: molecular dynamics of n-alkanes,” *J. Comput. Phys.* **23**, 327–341 (1977).

<sup>64</sup>H. C. Andersen, “Rattle: A “velocity” version of the shake algorithm for molecular dynamics calculations,” *J. Comput. Phys.* **52**, 24–34 (1983).

<sup>65</sup>S. Miyamoto and P. A. Kollman, “Settle: An analytical version of the shake and rattle algorithm for rigid water models,” *J. Comput. Chem.* **13**, 952–962 (1992).

<sup>66</sup>M. J. Frisch, G. W. Trucks, H. B. Schlegel, G. E. Scuseria, M. A. Robb, J. R. Cheeseman, G. Scalmani, V. Barone, G. A. Petersson, H. Nakatsuji, X. Li, M. Caricato, A. V. Marenich, J. Bloino, B. G. Janesko, R. Gomperts, B. Mennucci, H. P. Hratchian, J. V. Ortiz, A. F. Izmaylov, J. L. Sonnenberg, D. Williams-Young, F. Ding, F. Lipparini, F. Egidi, J. Goings, B. Peng,

A. Petrone, T. Henderson, D. Ranasinghe, V. G. Zakrzewski, J. Gao, N. Rega, G. Zheng, W. Liang, M. Hada, M. Ehara, K. Toyota, R. Fukuda, J. Hasegawa, M. Ishida, T. Nakajima, Y. Honda, O. Kitao, H. Nakai, T. Vreven, K. Throssell, J. A. Montgomery, Jr., J. E. Peralta, F. Ogliaro, M. J. Bearpark, J. J. Heyd, E. N. Brothers, K. N. Kudin, V. N. Staroverov, T. A. Keith, R. Kobayashi, J. Normand, K. Raghavachari, A. P. Ryndell, J. C. Burant, S. S. Iyengar, J. Tomasi, M. Cossi, J. M. Millam, M. Klene, C. Adamo, R. Cammi, J. W. Ochterski, R. L. Martin, K. Morokuma, O. Farkas, J. B. Foresman, and D. J. Fox, “Gaussian®16 Revision C.01,” (2016), Gaussian Inc. Wallingford CT.

<sup>67</sup>D. A. Case, H. M. Aktulga, K. Belfon, D. S. Cerutti, G. A. Cisneros, V. W. D. Cruzeiro, N. Forouzesh, T. J. Giese, A. W. Gotz, H. Gohlke, *et al.*, “Amber tools,” *J. Chem. Inf. Model.* **63**, 6183–6191 (2023).

<sup>68</sup>J. Wang, R. M. Wolf, J. W. Caldwell, P. A. Kollman, and D. A. Case, “Development and testing of a general amber force field,” *J. Comput. Chem.* **25**, 1157–1174 (2004).

<sup>69</sup>J. Wang, W. Wang, P. A. Kollman, and D. A. Case, “Automatic atom type and bond type perception in molecular mechanical calculations,” *J. Mol. Graph. Model* **25**, 247–260 (2006).

<sup>70</sup>I. S. Joung and T. E. Cheatham III, “Determination of alkali and halide monovalent ion parameters for use in explicitly solvated biomolecular simulations,” *The journal of physical chemistry B* **112**, 9020–9041 (2008).

<sup>71</sup>W. L. Jorgensen, J. Chandrasekhar, J. D. Madura, R. W. Impey, and M. L. Klein, “Comparison of simple potential functions for simulating liquid water,” *J. Chem. Phys.* **79**, 926–935 (1983).

<sup>72</sup>G. M. Torrie and J. P. Valleau, “Nonphysical sampling distributions in monte carlo free-energy estimation: Umbrella sampling,” *J. Comput. Phys.* **23**, 187–199 (1977).

<sup>73</sup>G. M. Torrie and J. P. Valleau, “Monte carlo free energy estimates using non-boltzmann sampling: Application to the sub-critical lennard-jones fluid,” *Chem. Phys. Lett.* **28**, 578–581 (1974).

<sup>74</sup>M. R. Shirts and J. D. Chodera, “Statistically optimal analysis of samples from multiple equilibrium states,” *J. Chem. Phys.* **129**, 124105 (2008).

<sup>75</sup>J. Jung, K. Yagi, C. Tan, H. Oshima, T. Mori, I. Yu, Y. Matsunaga, C. Kobayashi, S. Ito, D. Ugarte La Torre, *et al.*, “GENESIS 2.1: High-performance molecular dynamics software for enhanced sampling and free-energy calculations for atomistic, coarse-grained, and quantum mechanics/molecular mechanics models,” *J. Phys. Chem. B* **128**, 6028–6048 (2024).

<sup>76</sup>Y. Matsunaga, M. Kamiya, H. Oshima, J. Jung, S. Ito, and Y. Sugita, “Use of multistate bennett acceptance ratio method for free-energy calculations from enhanced sampling and free-energy perturbation,” *Biophys. Rev.* , 1–10 (2022).

<sup>77</sup>S. Doudou, N. A. Burton, and R. H. Henchman, “Standard free energy of binding from a one-dimensional potential of mean force,” *J. Chem. Theory Comput.* **5**, 909–918 (2009).

<sup>78</sup>A. A. Ojha, L. W. Votapka, and R. E. Amaro, “Advances and challenges in milestone simulations for drug–target kinetics,” *J. Chem. Theory Comput.* **20**, 9759–9769 (2024).